Model Tests on Lateral Bearing Behaviors of Cone-shaped Hollow Flexible Reinforced Concrete Foundation in Coarse Sand under Monotonic Lateral Load

Da-Yong Li[1], Hao Liang[1], Qian Xiang[2], Yu-Kun Zhang[2,*], Gang Tian[3], Hai-Jun Zhang[3]

[1]College of Pipeline and Civil Engineering, China University of Petroleum (East China), Qingdao, China

[2]School of Civil and Architectural Engineering, Shandong University of Science and Technology, Qingdao, China

[3]C+E Center for Engineering Research Test and Appraisal Co., Ltd., Beijing, China

Received 22 October 2025; received in revised form 11 January 2026; accepted 19 January 2026

DOI: https://doi.org/10.46604/ijeti.2026.15816

Abstract

With the rapid increase in installed onshore wind turbine capacity, greater lateral bearing capacity of foundations is required. The cone-shaped hollow flexible reinforced concrete foundation (CHFRF) is proposed. Model tests and numerical simulations are conducted to investigate the lateral bearing behavior of the CHFRF in coarse sand. The results indicate that the lateral bearing capacity of CHFRF increases with the aspect ratio and decreases with loading eccentricity. Compared with a circular foundation with the same height, the CHFRF with a diameter of 400 mm exhibits an average increase of 17.6% in lateral bearing capacity while using only 65% of the concrete volume. The rotation center is located at 0.5–0.65 times the foundation height. Based on the earth pressure distribution at the limit state and the limit equilibrium method, a theoretical approach for predicting the CHFRF lateral bearing capacity is proposed.

Keywords: wind turbine, cone-shaped hollow flexible reinforced concrete foundation, lateral bearing capacity, rotation center, earth pressure

1. Introduction

Wind energy, as a renewable energy source, has developed rapidly worldwide. In recent years, onshore wind turbines have been gradually evolving towards larger sizes and higher wind speeds. In 2024, a 10 MW onshore wind turbine was officially connected to the power grid for operation [1]. The lateral loads increase with the increasing installed capacity of onshore wind turbines. The bearing capacity of wind energy foundations is crucial for structural safety and operational efficiency. Depending on the geological conditions of various engineering sites, piles and gravity-based foundations can be selected. When the soil strength (e.g., coarse sand) is sufficient to support the wind turbine, gravity-based foundations are the preferred choice [2]. Gravity-based foundations resist the bending moments caused by lateral loads through their self-weight. The volume of concrete required for the gravity-based foundations of 1.8 MW and 2.3 MW wind turbines is 382 m³ and 542 m³, respectively [3]. This indicates that the installation of the gravity-based foundation requires a large volume of concrete.

However, under high lateral loads, gravity-based foundations are prone to slippage and uneven settlement, which may cause overturning failure of the wind turbine [4]. Ensuring stability thus often requires a larger foundation volume, increasing material costs. Additionally, excavation of large-diameter pits in sandy soils necessitates substantial wall support to prevent deformation, further raising construction time and expense [5]. In order to overcome the above-mentioned disadvantages of

* Corresponding author. E-mail address: philc007@163.com

mountain wind turbine foundations and to increase the foundation bearing capacity and flexibility, an innovative type of mountain wind turbine foundation, the cone-shaped hollow flexible reinforced concrete foundation (CHFRF), has been proposed [7].

As shown in Fig. 1, a cone-shaped foundation pit is first excavated, and the inclined foundation pit wall can effectively reduce the risk of collapse. The extracted rubble and soil are stacked beside the pit. The pit wall is then covered by a rubber layer to serve as the flexible layer. The rubber layer beneath the CHFRF increases the foundation flexibility to resist cyclic and dynamic loadings and to increase the bearing capacity. The CHFRF is allowed to rotate slightly with the allowable degree under cyclic wind loads and to release the huge moment acting on the foundation, leading to an increase in wind turbine stability [6]. After the foundation pit excavation is completed, the reinforced concrete side walls and bottom plates of the CHFRF are poured. The internal hollow structure can significantly reduce the volume of concrete used in the CHFRF. The excavated soil from the foundation pit will be backfilled into the internal hollow of the CHFRF, which can increase the self-weight of the foundation and reduce the volume of discarded soil. Finally, the lid of the CHFRF is poured.

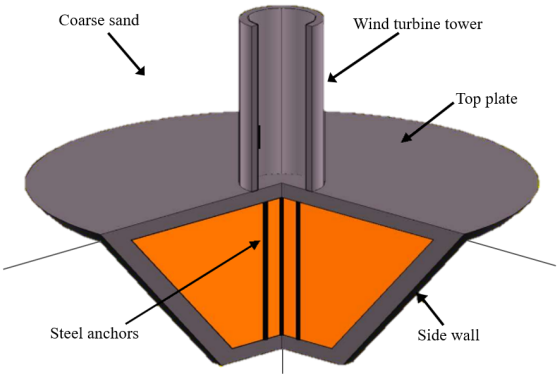

Fig. 1 Sketch of the CHFRF

Both the gravity-based foundation and the CHFRF belong to the category of shallow foundations; thus, the study results of the gravity-based foundation can be referenced. Sethy et al. [7] carried out model tests in sand to investigate the relationship between the embedded ratio and the rotation center of the gravity-based foundation under inclined loads. Results show that the rotation center of the gravity-based foundation moves downwards with increasing the embedded ratio. Additionally, based on the test results, a reduction factor method was proposed to predict the ultimate inclined load.

Deng et al. [8-9] conducted model tests to study the bearing behavior of shallow foundations and found that the lateral displacement, settlement value, and contact pressures under the foundation increase with the increase of the lateral load. The contact pressures under the foundation increase in the direction of the lateral load under monotonic loading. However, under dynamic loads, the contact pressures under the foundation exhibit significant uneven variations. El-Wakil et al. [10] point out that the earth pressure and friction force provide the resistance during lateral loading. Therefore, the lateral bearing capacity increases with increasing plastic failure range and interface roughness. Cerato et al. [11] found that the lateral bearing capacity of the gravity-based foundation increases with the foundation stiffness and the foundation size.

The shape of the CHFRF differs significantly from that of the gravity-based foundation. Some studies have explored the bearing behavior of the CHFRF. Li et al. [12] verified through model experiments that under the same load conditions, the lateral bearing capacity of the CHFRF increased by approximately 33.5% than that of the gravity-based foundation. The volume of concrete used in the CHFRF was only 20% of that used in the gravity-based foundation under the same lateral load. Li et al. [13] carried out a model test to investigate the behavior of the rotation center of the CHFRF. Under the ultimate state, the distance between the rotation center and the foundation lid is 0.6 to 0.65 times the foundation length, and the distance between the rotation center and the foundation centerline is 0.15 to 0.18 times the foundation diameter.

Zhang et al. [14] performed model tests to study the earth pressure distribution around the CHFRF. Results show that the earth pressure approximately follows an inverted triangular distribution along the depth of the foundation. Additionally, the range of the passive earth pressure zone decreases with increasing load. Li et al. [15] conducted numerical simulations to investigate the lateral bearing behavior of the prototype CHFRF. The ultimate lateral bearing capacity increased with the increase in the CHFRF aspect ratio. Furthermore, the effect of the scale on the lateral bearing capacity of the CHFRF can be ignored. Li et al. [16] proposed a theoretical method for predicting the lateral bearing capacity of the CHFRF based on the distribution of the earth pressure. However, this method assumes that the incremental earth pressure presents a quadratic function distribution at the front and rear sidewalls and that the rotation center is always located at the center of the base plate. These assumptions differ from practical conditions.

In practical engineering, the CHFRF is made of reinforced concrete, and the concrete will suffer from cracking damage under long-term loading. As damage accumulates, the material stiffness decreases, and the nonlinearity of the stress-strain curve becomes more pronounced [17-21]. In this paper, the stiffness of the 1-g model tests is greater than that of the prototype and can be treated as rigid. Therefore, steel CHFRFs are employed instead of reinforced concrete CHFRFs.

Although previous studies have extensively investigated the lateral bearing capacity, rotation center, and earth pressure distribution of CHFRFs, the influence of foundation diameter and loading eccentricity on rotation center variation has not been fully clarified. The theoretical method for predicting the lateral bearing capacity of the CHFRF in previous studies needs to be further improved. This paper conducts model tests and numerical simulations to investigate the lateral bearing behavior of the CHFRF. The key innovation points are as follows: (i) exploring the influence of CHFRF aspect ratio and loading eccentricity on lateral bearing capacity; (ii) clarifying the variation of the CHFRF rotation center and passive earth pressure distribution under different aspect ratios and loading eccentricities; (iii) based on the variations in rotation center and earth pressure distribution, a theoretical method for predicting the ultimate lateral bearing capacity of the CHFRF that considers passive soil pressure both in front of and behind the foundation is proposed; (iv) the influence of the scale effect on the lateral bearing behavior of the CHFRF is obtained.

2. Model Test

Model tests were carried out to study the lateral bearing characteristics of cone-shaped hollow flexible reinforced concrete foundations (CHFRF) in coarse sand. The effects of foundation diameter and loading eccentricity on the lateral ultimate bearing capacity, position of the rotation center, and earth pressure distribution were analyzed.

2.1 Test Setup

(1) The model test tank

The model tests were conducted in a cylindrical tank measuring 1.0 m in diameter and 1.5 m in height (Fig. 2). The ratio of the diameter of the cylindrical tank to that of the CHFRF is approximately 3.5 [7], which is sufficient to eliminate boundary effects.

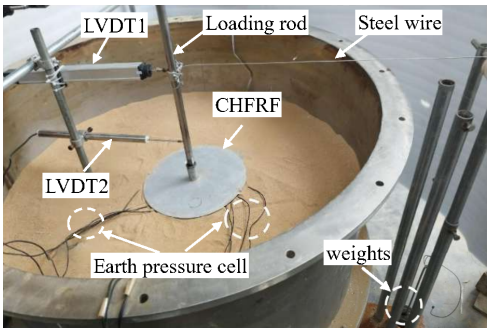

Fig. 2 Model test setup

(2) The CHFRF and circular foundation models

The dimensions of the Cone-shaped Hollow Flexible Reinforced Concrete Foundation (CHFRF) in this paper are converted from those of a circular gravity-based foundation with the same height. The dimensions of the circular foundation are scaled down from a 2 MW mountainous wind turbine foundation in Qingdao, China. The diameter and height of the prototype of the circular foundation are 15 m and 3 m, respectively. In addition, the scale between the model and the prototype is 1:50. The CHFRF and circular foundation models were manufactured using steel (Fig. 3), and the corresponding diameters and heights are listed in Table 1. In the model test, a loading rod was fixed to the top plates of the CHFRF and the circular foundation. Lateral loads and moments with different constant ratios were applied at the center of the top plate by varying the eccentricities of loading.

Table 1 Dimension of CHFRF and circular foundation

Nos. of foundation	Top plate diameter D(mm)	Base plate diameter D_1 (mm)	Height H_1(mm)	Aspect ratio (D/H_1)
CHFRF-I	300	0	60	5
CHFRF-II	350	0	60	5.83
CHFRF-III	400	0	60	6.67
Circular foundation	300	300	60	5

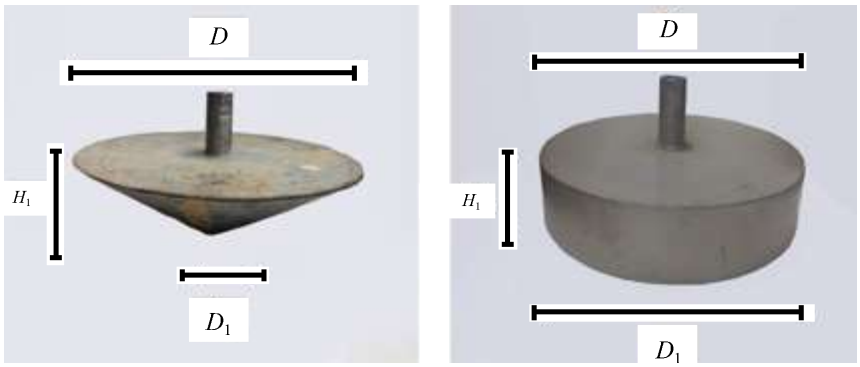

(a) CHFRF model (b) Circular foundation

Fig. 3 Foundation models

(3) Sand used

The coarse sand is collected from an onshore wind farm, and its unit weight γ and internal friction angle ϕ are 17 kN/m^3 and 38°, respectively. It can be seen from Fig. 4 that the particle diameter is within the range of 0.25 to 8 mm. The maximum void ratio e_{max}, and the minimum void ratio e_{min} of the sand are 1.102 and 0.663, respectively. The initial relative compactness D_r of the sand was 0.52, which is medium dense sand. The average particle diameter D_{50} approximately equals 1 mm. The unevenness coefficient C_u and the curvature coefficient C_c are 6.17 and 1.6, respectively. This sand is poorly graded medium-coarse sand.

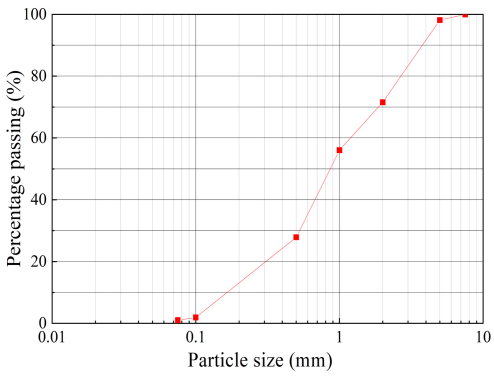

Fig. 4 Particle size distribution curve

(4) Measuring device

The displacement and earth pressure are measured by two displacement transducers (LVDT1 and LVDT2) and eight earth pressure cells (EPC). As shown in Fig. 5, both LVDT1 and LVDT2 are horizontally mounted with the loading rod. The height of the LVDT1 is consistent with the loading eccentricity, and LVDT2 is positioned 15 cm above the top plate. The EPCs are fixed at the front and rear side walls of the CHFRF, with corresponding embedded depths of 0, 0.33, 0.67, and 1 time the foundation height, respectively. A data acquisition device is connected to the LVDTs and EPCs to record the displacement and earth pressure.

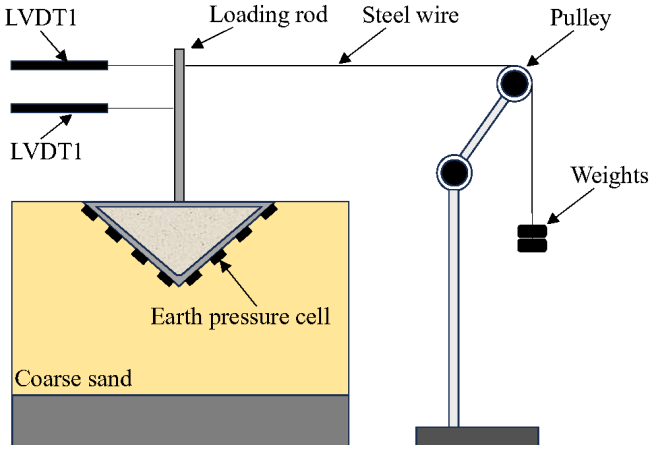

Fig. 5 Layout of the model test

2.2 Test Procedure

To ensure the homogeneity of the sand in the test, the sand was prepared by the method of layer-by-layer filling and compaction. The filling height for each layer was 10 cm. The compactness coefficient λ_c is used in the Code for Design of Building Foundations of China [22] to measure the compaction effect of the backfill soil, and λ_c should be greater than 0.97. λ_c is defined as the ratio of P_d to P_{dmax}, where P_d is the initial dry density and P_{dmax} is the maximum dry density. P_d is calculated using the initial void ratio, and P_{dmax} is obtained from compaction test results. In this paper, the compactness coefficient is 0.974, indicating that the compaction effect of the sand meets the requirements. The coarse sand is first scattered and compacted in the cylindrical tank until its height reaches 1.2 m, and then the CHFRF model, LVDTs, and EPCs are installed at the specified location, respectively. Finally, the sand surrounding the CHFRF model is continuously hit 20 times by a hammer to ensure the relative density [23].

Monotonic lateral loading model tests are conducted under different loading eccentricities. In the study, the load eccentricity is normalized as H/H_1, where the load eccentricity H presents the distance from the loading position to the top plate, and H_1 is the foundation height. The lateral loads are applied to the CHFRF by gradually increasing the standard weights. The incremental load of each step is 3.92 N. When the lateral displacement change rate is less than 0.01 mm/10 minutes at a certain load step, it can be considered that the stable state for this load step has been reached. The load value and the current reading of the horizontal displacement sensor are then recorded. Then the next step load is applied. The ultimate bearing capacity is obtained when the foundation lateral displacement reaches 0.05D. The maximum value of the lateral load is defined as the ultimate bearing capacity. After the lateral loading was completed, the sand in the range of 2 times the embedded depth was loosened and the CHFRF model was installed at the specified location to conduct other loading conditions.

Fig. 6 gives the results of the repeated tests on the lateral bearing capacity. The load eccentricity of the parallel test is $H/H_1 = 5$, and the aspect ratios of the foundation are $D/H_1 = 5$ and 6.67. Results show that the test error was within 5%, indicating that the test method is feasible.

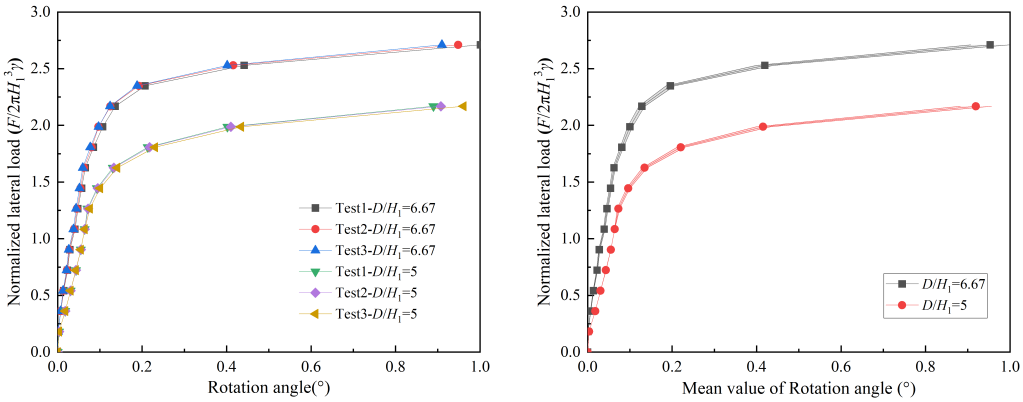

(a) Lateral bearing capacity of the repeated tests (b) Error bands of the repeated tests

Fig. 6 Results of the repeated tests

3. Test Results and Analysis

The study indicates that the normalized model test results can provide a reference to practical engineering [24]. In the study, the lateral loads and the moment are normalized as $F/2\pi H_1^3\gamma$ and $M/2\pi H_1^4\gamma$, where F and M represent the lateral loads and moments acting on the CHFRF, respectively [25].

3.1 Parametric Study of Lateral Bearing Capacity

The rotation center is normalized as x/H_1, where x represents the distance from the rotation center to the top plate. The rotation angle α can be calculated by

$$\alpha = \arctan\frac{x_1}{H} \tag{1}$$

where x_1 is the lateral displacement measured by the LVDT1. In addition, the embedded depth can be normalized as the l/H_1, where l is the distance between the embedded depth and the top plate of the foundation.

The normalized lateral loads under the different loading eccentricities (H/H_1 = 4 to 7) are drawn in Fig. 7. The lateral bearing capacity increases to a constant value with increasing rotation angle. The bearing capacity of the CHFRF has a positive correlation with its aspect ratios D/H_1. This is because the contact areas between the front and rear side walls and sand increase with increasing aspect ratios, causing more soil to be mobilized to resist lateral loads. Additionally, the study found that the CHFRF has advantages in lateral bearing capacity compared with the circular foundation with the same height. Taking CHFRF-III as an example, the lateral bearing capacity increases by an average of 17.6% compared to that of the circular foundation (Volume ratio of CHFRF-III to the circular foundation $V_{\text{CHFRF-III}}/C_{\text{ircle}}$ = 0.65) under the same loading eccentricities, proving that the CHFRF not only reduces the construction cost but also improves the lateral bearing capacity.

Fig. 8 shows the ultimate lateral loads against the moment curves. The moment loads of the CHFRF decrease linearly as the lateral loads increase, but increase as the aspect ratios increase. When the normalized lateral loads exceed 1.82, the moment loads of the circular foundation are larger than those of the CHFRF-I, but decrease by 8.6% and 13% compared with the CHFRF-II and the CHFRF-III. In addition, the failure envelope of the CHFRF can be fitted using a linear function, while that of the circular foundation requires a cubic polynomial. This indicates that the failure mode of the CHFRF differs from that of the circular foundation. The area under the fitted failure envelope curve of the CHFRF is greater than that of the circular foundation at the same diameter and height, demonstrating that the bearing capacity of the CHFRF exceeds that of the circular foundation under combined loading.

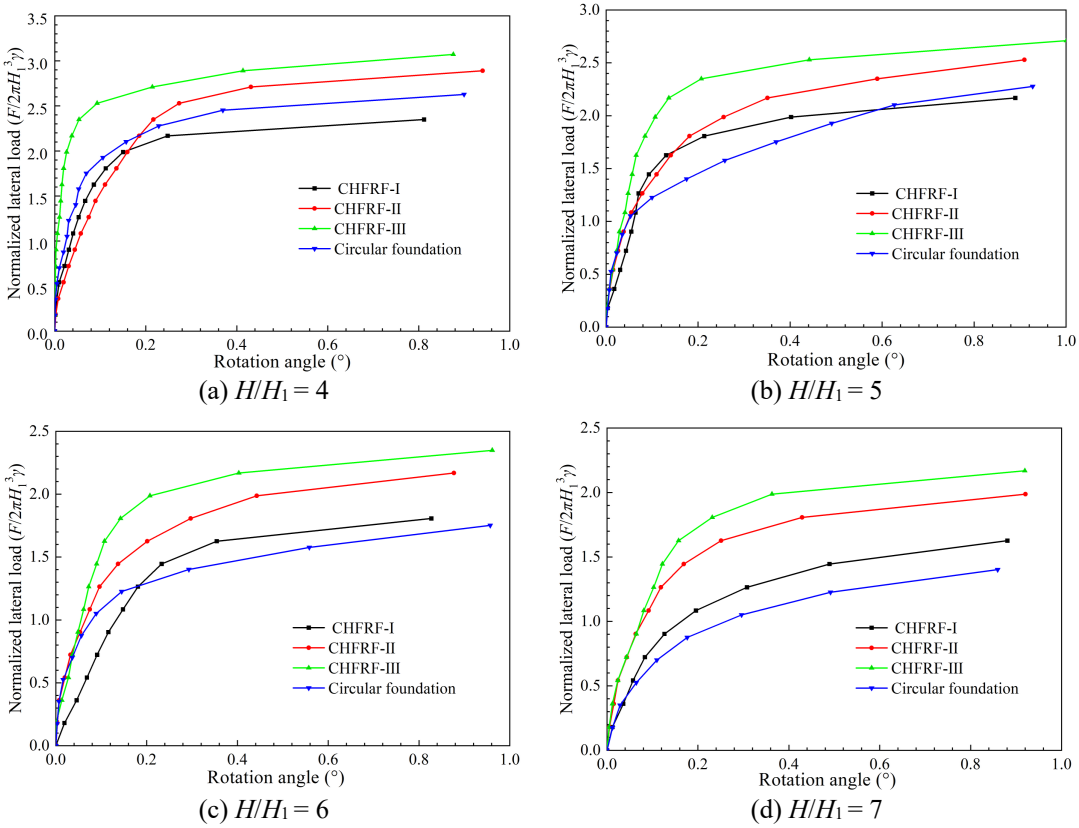

(a) $H/H_1 = 4$ (b) $H/H_1 = 5$

(c) $H/H_1 = 6$ (d) $H/H_1 = 7$

Fig. 7 The normalized lateral load against rotation angle

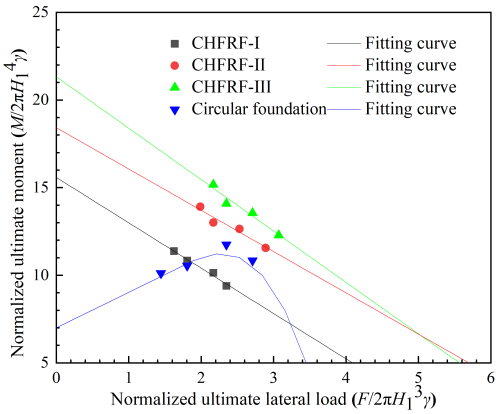

Fig. 8 The dimensionless lateral loads against moments

3.2 Rotation Center of the CHFRF

The position of the rotation center can be calculated by [26]:

$$x = \frac{ax_1 - bx_2}{b - a} \tag{2}$$

where x_1 and x_2 represent the lateral displacements measured by the LVDT1 and LVDT2, respectively. Parameters a and b represent the distance from LVDT1 and LVDT2 to the top plate, respectively.

Fig. 9 shows the movement of the rotation center under the various loading eccentricities. In the initial stage, the rotation center moves slightly upward, and then its movement trend gradually increases as the rotation angle increases. The range of the corresponding values is from 0.7 H_1 to 0.9 H_1. After the rotation angle exceeds 0.4°, the rotation center moves upward rapidly. Finally, the CHFRF becomes unstable and fails when the rotation center moves to 0.5 H_1 to 0.65 H_1.

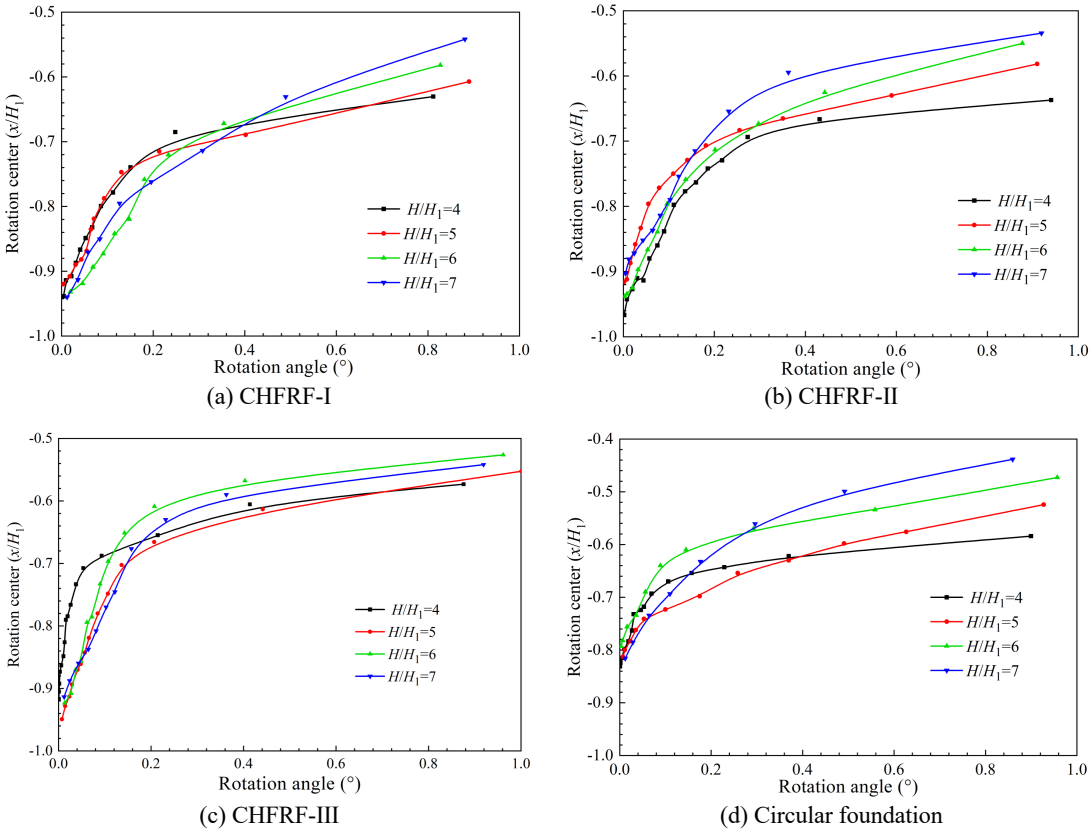

Fig. 9 Relationships between the rotation center and rotation angle

Under the limiting condition, the rotation center of the CHFRF with different aspect ratios are shown in Fig. 10. The normalized distance between the rotation center and the top plate, x/H_1, decreases with increasing the loading eccentricity and aspect ratios. The results demonstrate that the failure mode of the CHFRF changes from the translation movement to rotation with increasing the loading eccentricity and aspect ratios. The passive earth pressure and frictional resistance at the bottom of the CHFRF resist the lateral load applied at the loading point. As the rotation center moves upward along the embedded depth, the passive earth pressure area and the frictional resistance in front of the CHFRF decrease, leading to a decrease in the lateral bearing capacity. Therefore, the rotation center should be kept as low as possible in practical engineering design.

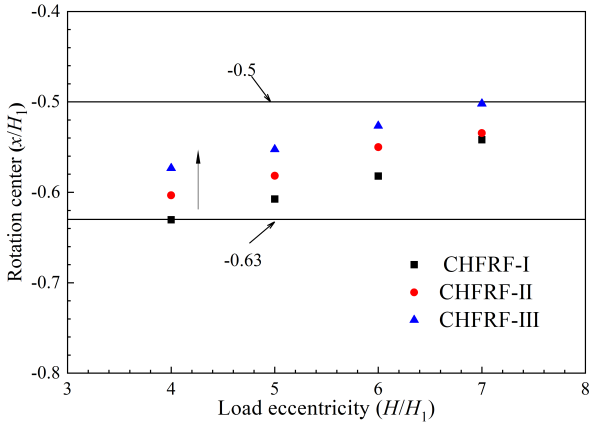

Fig. 10 Relationship between rotation center and loading eccentricities

3.3 Distribution Law of Earth Pressure

Taking loading eccentricity $H/H_1 = 5$ as an example, the distribution of the incremental earth pressure for the CHFRF-I, II, and III is drawn in Figs. 11 to 13. As shown in Figs. 11 to 13(a), the incremental earth pressure in the range of 0~0.6H_1 is positive at the front sidewall, and linearly decreases with increasing the embedded depth l, indicating that the passive earth

pressure acts on the sidewall. Previous studies reveal that the position where the incremental earth pressure equals zero is regarded as the rotation center [14]. Therefore, the rotation center is approximately equal to $0.6H_1$. The result agrees well with the rotation center determined by Eq.2. The incremental earth pressure reduces to negative values as the embedded depth l continuously increases, demonstrating the active earth pressure acting on the side wall in the range of 0.6 to 1 H_1. Furthermore, the incremental earth pressure increases as the aspect ratio increases, and the maximum values for the CHFRF-I, II, and III are 13.2 kPa, 17.3 kPa, and 20.2 kPa, respectively.

As shown in Figs. 11 to 13(b), the incremental earth pressure in the range of 0 to $0.6H_1$ is negative at the rear sidewall and first decreases, then increases as the embedded depth l increases. The reason is that the CHFRF moves laterally and rotates towards the loading direction, thereby reducing the earth pressure at the rear sidewall. Note that there is no contact between the sidewall and soils when incremental earth pressure decreases to a constant value during lateral loading. The incremental earth pressure in the range of 0.6 to 1 H_1 is positive, and linearly increases with increasing embedded depth l. The results demonstrate that the sidewall of CHFRF and the sand in the passive zone are further squeezed because the CHFRF rotates towards the loading direction.

It is found that the failure mechanism of the CHFRF is similar to that of the circular foundation [27]. A calculation method of the lateral bearing capacity for the CHFRF is proposed by referring to the method for the circular foundation. The details are described in Section 4.

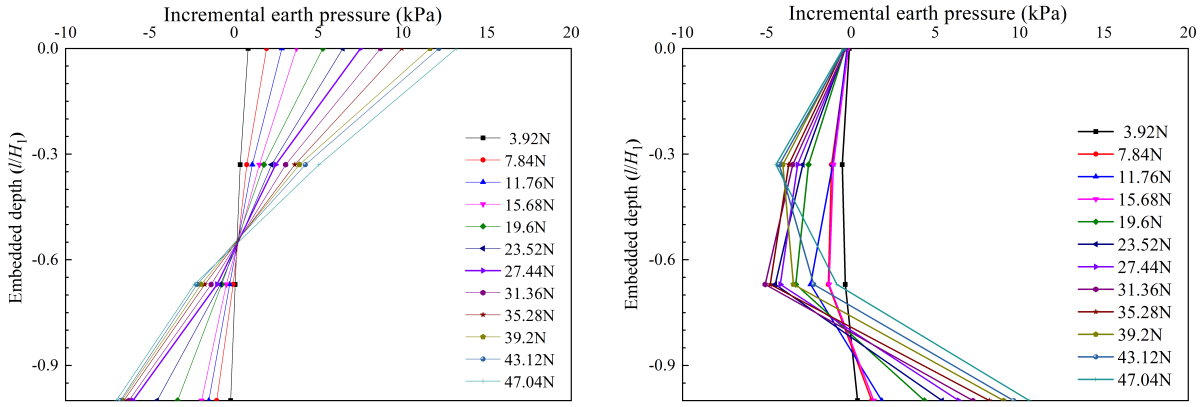

(a) At the front sidewall (b) At the rear sidewall

Fig. 11 Incremental earth pressure distribution of CHFRF-I

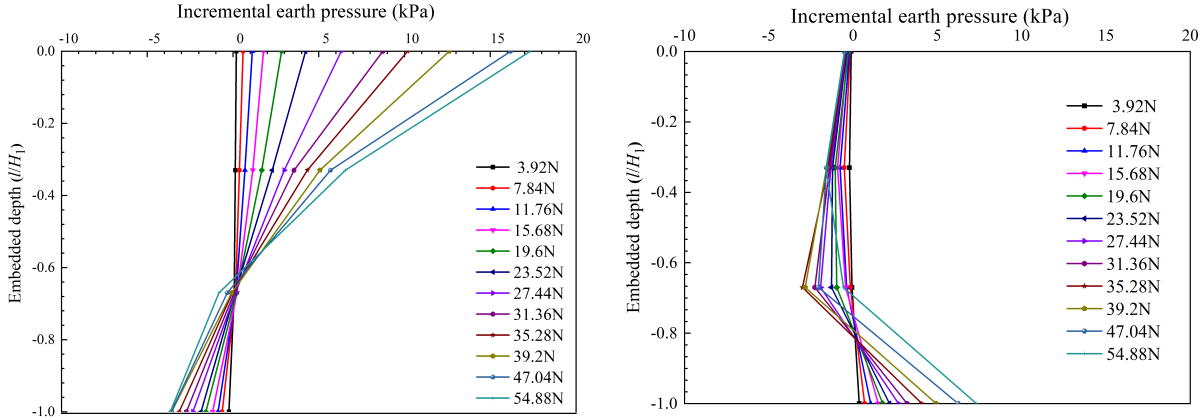

(a) At the front sidewall (b) At the rear sidewall

Fig. 12 Incremental earth pressure distribution of CHFRF-II

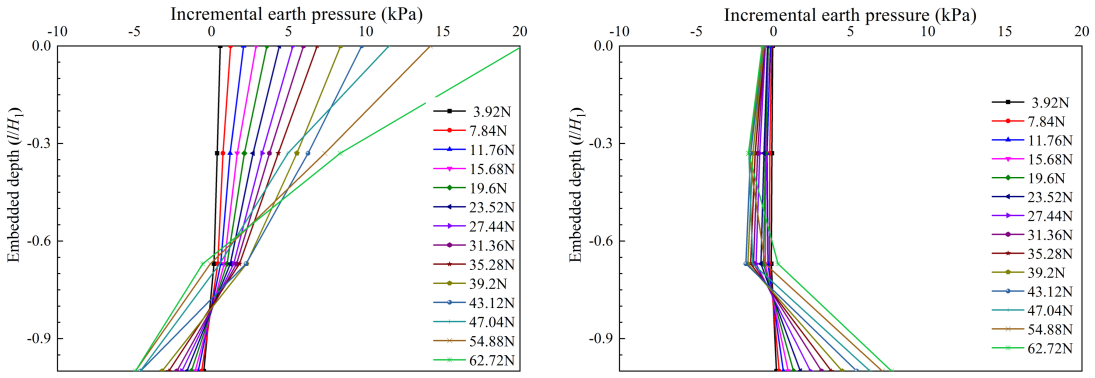

(a) At the front sidewall (b) At the rear sidewall

Fig. 13 Incremental earth pressure distribution of CHFRF-III

4. Calculation for lateral bearing capacity

Based on the model test results, the relationships among the ultimate lateral bearing capacity, the position of the rotation center, and the earth pressure distribution are obtained. Consequently, a theoretical method for predicting the ultimate lateral bearing capacity of the CHFRF can be proposed.

4.1 Method of Calculating the Lateral Bearing Capacity for the CHFRF

The earth pressure and the corresponding frictional force acting on the CHFRF are shown in Fig. 14. The calculation method is based on the following assumptions.

(1) In the *xoz* plane, the resistance is defined as positive when its direction is right and upward. The moment is positive along the clockwise direction.

(2) In the active earth pressure zone, the stresses on the side wall are not considered since the sidewall and sand separate during loading. In the passive earth pressure zone, the stresses on the sidewall decrease linearly with increasing embedded depth *l*.

(3) In the *xoy* plane, the earth pressure follows Winkler's assumption in the circumferential direction.

In the *xoz* plane, the passive earth pressure can be expressed as

$$\sigma = \rho\omega k_v = \frac{l_0 - l}{\cos\beta}\omega k_v \tag{3}$$

where l_0 is the vertical distance from the rotation center to the top plate of the CHFRF, β is the angle between the sidewall and central axis, ω is the rotation angle of the CHFRF, and k_v is the vertical reaction coefficient, which can be determined using the plate loading test.

In the *xoy* plane, the passive earth pressure along the circumferential direction, σ_β, is calculated by

$$\sigma_\beta = \rho\omega k_v \cos\theta = \frac{l_0 - l}{\cos\beta}\omega k_v \cos\theta \tag{4}$$

In the *xoy* plane, the passive earth pressure along the circumferential direction can be divided along the *x-axis* direction. The formula is presented as

$$\sigma_\theta = \rho\omega k_v \cos^2\theta = \frac{l_0 - l}{\cos\beta}\omega k_v \cos^2\theta \tag{5}$$

In the *xoz* plane, σ_θ can be divided into the *x-axis* and *z-axis* directions. The component along the *x-axis* direction $\sigma_{\theta x}$ is computed by:

$$\sigma_{\theta x} = \rho\omega k_v \cos^2\theta\cos\beta = \frac{l_0 - l}{\cos\beta}\omega k_v \cos^2\theta\cos\beta \tag{6}$$

At the front side walls of the CHFRF, the component along the *z-axis* direction is shown as

$$\sigma_{\theta z1} = -\rho\omega k_v \cos^2\theta\sin\beta = -\frac{l_0 - l}{\cos\beta}\omega k_v \cos^2\theta\sin\beta \tag{7}$$

At the rear side wall of the CHFRF, the component along the *z-axis* is expressed as

$$\sigma_{\theta z2} = \rho\omega k_v \cos^2\theta\sin\beta = \frac{l_0 - l}{\cos\beta}\omega k_v \cos^2\theta\sin\beta \tag{8}$$

At the front side wall of the CHFRF, the components of the corresponding frictional force along the *x* and *z-axis* directions can be respectively calculated as

$$\tau_{x1} = -\lambda\sigma_{\theta x} = -\lambda\frac{l_0 - l}{\cos\beta}\omega k_v \cos^2\theta\sin\beta \tag{9}$$

$$\tau_{z1} = -\lambda\sigma_{\theta z1} = -\lambda\frac{l_0 - l}{\cos\beta}\omega k_v \cos^2\theta\cos\beta \tag{10}$$

where the λ is the friction factor between the CHFRF and sand.

At the rear side wall of the CHFRF, the component of the corresponding frictional force along the *x* and *z-axis* directions is expressed as

$$\tau_{x2} = \lambda\sigma_{\theta x} = \lambda\frac{l_0 - l}{\cos\beta}\omega k_v \cos^2\theta\sin\beta \tag{11}$$

$$\tau_{z2} = -\lambda\sigma_{\theta z2} = -\lambda\frac{l_0 - l}{\cos\beta}\omega k_v \cos^2\theta\cos\beta \tag{12}$$

The moment rotation about center O_1 is caused by the passive earth pressure and the corresponding frictional force. The moment induced by the passive earth pressure is calculated as

$$M_1 = 2\left(\int_0^{\frac{\pi}{2}}\int_{l_0}^{H_1}\sigma_{\theta x} l\tan\beta d\theta dl + \int_{\frac{\pi}{2}}^{\pi}\int_0^{l_0}\sigma_{\theta x} l\tan\beta d\theta dl\right)(l - l_0) \tag{13}$$

$$M_2 = 2\left(\int_{\frac{\pi}{2}}^{\pi}\int_0^{l_0}\sigma_{\theta z2} l\tan\beta d\theta dl - \int_0^{\frac{\pi}{2}}\int_{l_0}^{H_1}\sigma_{\theta z1} l\tan\beta d\theta dl\right) l\tan\beta \tag{14}$$

The moment induced by the corresponding frictional force can be expressed as

$$M_3 = 2\left(\int_0^{\frac{\pi}{2}}\int_{l_0}^{H_1}\tau_{x1} l\tan\beta d\theta dl + \int_{\frac{\pi}{2}}^{\pi}\int_0^{l_0}\tau_{x2} l\tan\beta d\theta dl\right)(l - l_0) \tag{15}$$

$$M_4 = 2\left(\int_{\frac{\pi}{2}}^{\pi}\int_0^{l_0}\tau_{z2} l\tan\beta d\theta dl - \int_0^{\frac{\pi}{2}}\int_{l_0}^{H_1}\tau_{z1} l\tan\beta d\theta dl\right) l\tan\beta \tag{16}$$

The moment caused by the external loads can be computed as

$$M_5 = (H + H_1 - l_0)F \tag{17}$$

The moment caused by the external loads equals the resisting moment during lateral loading. Therefore, the lateral bearing capacity F can be determined by:

$$F = -\frac{M_1 + M_2 + M_3 + M_4}{H + H_1 - l_0} \tag{18}$$

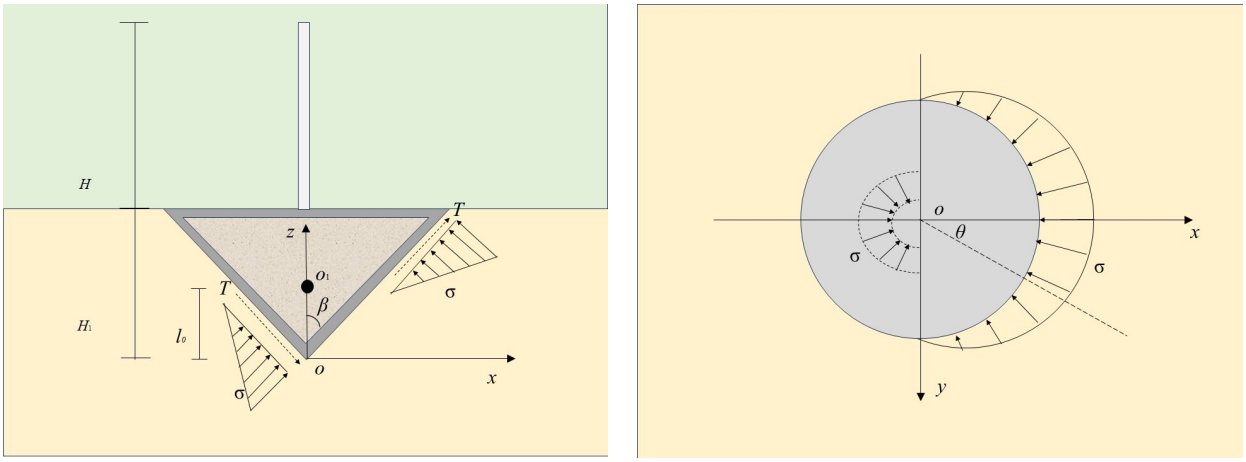

(a) Elevation view (b) Top view

Fig. 14 Earth pressure distribution of the CHFRF

4.2 Verification for the Proposed Method

In the case of the loading eccentricity of $H/H_1 = 5$, the diameters D of the CHFRF-I, II, and III are 0.3 m, 0.35 m, and 0.4 m, respectively. The heights of the CHFRF-I, II, and III are 0.06 m. The angles of the side wall β are 68.2°, 71.1°, and 73.3°, respectively. The value of ω is 0.02 rad. According to the Chinese technical code (GB50307-2012), the values of k_v for coarse sand range from 25 to 45 MPa/m. Therefore, k_v is conservatively determined to be 25 MPa/m [28]. It can be known from the model test that the rotation center is located at approximately 0.6 H_1 under the limiting condition. Therefore, the value of l_0 here is 0.024 m. All parameters are listed in Table 2. In terms of the above parameters, the ultimate bearing capacity of CHFRF-I, II, and III can be calculated by Eqs. (13)-(18).

Table 2 The parameters of ultimate lateral bearing capacity for CHFRFs

Nos. of foundation	Angle of side wall β (°)	Rotation angle of CHFRF ω (rad)	Vertical reaction coefficient kv (MN/m-3)	Vertical distance between the rotation center to the base plate of the CHFRF l0 (m)	friction factor λ
CHFRF-I	68.2	0.02	25	0.024	0.4 [22]
CHFRF-II	71.1				
CHFRF-III	73.3				

The ultimate lateral bearing capacities of CHFRF-I, II, and III are shown in Table 3. The results calculated by the theoretical method are always lower than the model test results. This indicates that the theoretical method is safer than the model test. The results show that the maximum error between the model test data and the calculation result is 7.2%, which proves that the method is reliable.

Table 3 The model test and calculation results

Nos. of	Normalized lateral bearing capacity $F/2\pi H_1^3\gamma$		
	Model test data	Calculation method	Relative error
CHFRF-I	2.17	2.01	7.2%
CHFRF-II	2.53	2.36	6.7%
CHFRF-III	2.71	2.53	6.6%

Based on the distribution of passive earth pressure around the CHFRF and the variation of the rotation center position under lateral loading, this paper proposes a theoretical method for determining the lateral ultimate bearing capacity. As shown in Table 4, the passive earth pressure on the loading side is divided into portions above and below the rotation center, which better reflects actual conditions.

Table 4 Comparison of errors from different theoretical methods

Reference	Remarks	Minimum error
This paper	The passive earth pressure distribution is determined by the rotation center location, which is difficult to ascertain.	6.6%
Li et al. [17]	Assuming that the soil pressure on the loading side of the foundation is linearly distributed, the soil pressure distribution on the rear side of the foundation is ignored.	7.99%
Zhang et al. [15]	The lateral bearing capacity of the foundation is calculated using the separation area method, while the distribution of soil pressure on the rear side of the foundation is ignored.	4.5%

5. Numerical Simulations of Scale Effect on the Lateral Bearing Capacity

Although the normalized method is used in this paper, the stress state of the model test sand and the stiffness of the foundation differ from those in the field test. Numerical simulations were conducted using the finite element software ABAQUS to apply the results of both the model test and the theoretical method to the prototype.

5.1 Numerical Simulation Model

The numerical simulations were conducted to investigate the influence of the scale effect on the lateral bearing capacity of the CHFRF. Fig. 15 gives the finite element model. To eliminate the boundary effect, the calculation range of the sand is selected as 10 times the diameter of the CHFRF, and the height is 5 times the diameter of the CHFRF.

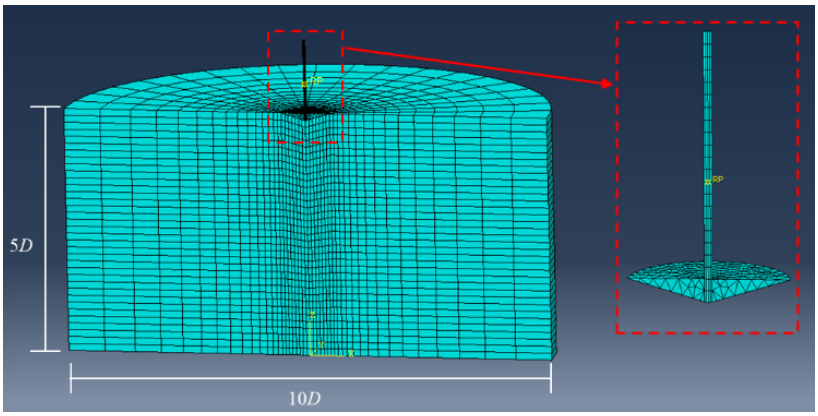

Fig. 15 Finite element model

The sand soil adopts the Mohr-Coulomb criterion. The γ and the friction angle of the sand are the same as the model tests. The elastic modulus and Poisson ratio are obtained through the back analysis from the model test results. The parameters of sand and the CHFRF are given in Table 5. The dimensions of the CHFRF at various scales are given in Table 6. The friction coefficient between the CHFRF and the sand is 0.5.

Table 5 Parameter of sand and foundation

Scale ratio	E_{sand} (MPa)	$E_{foundagtion}$ (GPa)	γ_{sand} (kN/m3)	μ_{sand}	$\mu_{foundation}$	φ (°)	Lateral load of each step(N)
1:50	1.5	6	17	0.3	0.2	28	4
1:10	7.5	30	17	0.3	0.2	28	500
1:1	75	300	17	0.3	0.2	28	500000

Table 6 CHFRF dimensions under different scales

Scale ratio	Top plate diameter D(m)	Height H_1(m)	Aspect ratio (D/ H_1)
1:50	0.4	0.06	6.67
1:10	2	0.3	6.67
1:1	20	3	6.67

To accurately reproduce the actual geostatic stress state of the prototype sand, the numerical simulation includes two steps: the geostatic analysis step and the loading analysis step. After the geostatic analysis was completed, the geostatic stress state can respond to the actual situation when the vertical displacement of the sand is less than 10^{-4} m (as shown in Fig. 16). The lateral loads are carried out on the CHFRF by gradually increasing the standard weights, same as the model test. The ultimate bearing capacity is obtained when the foundation lateral displacement reaches 0.05D.

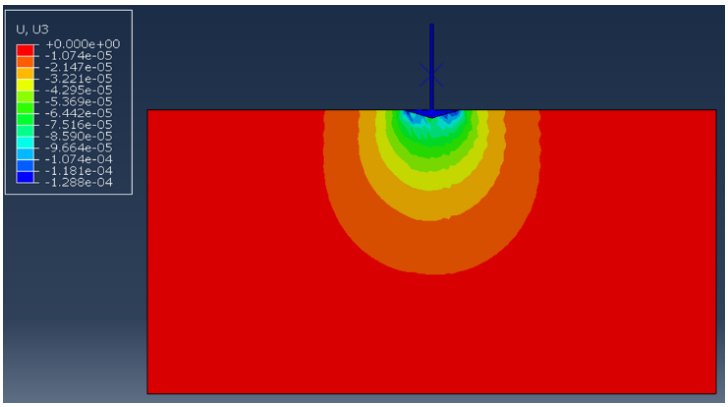

Fig. 16 Geostatic analysis result

Fig. 17 shows a comparison between the model test and simulation results under the normalized load eccentricities of 4, 5, 6, and 7. The results of the numerical simulations are in good agreement with the model test results, indicating that the numerical analysis results are reliable.

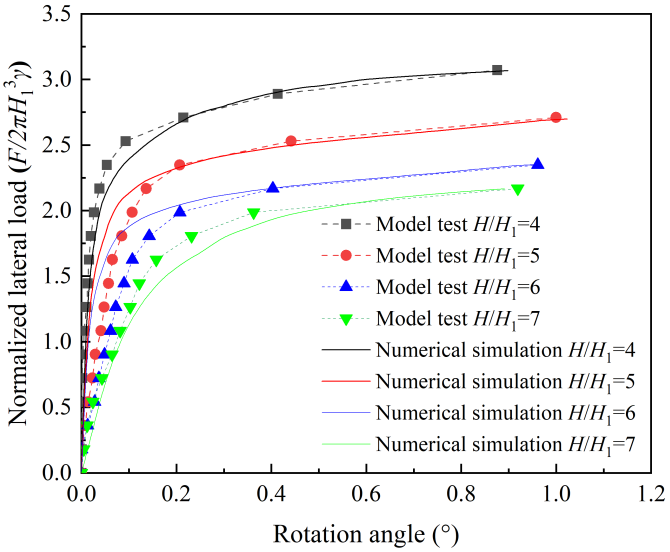

Fig. 17 Validation of the numerical simulation results

5.2 Scaling Analysis Results of the Numerical Simulations

The relationship between the rotation angle and the normalized lateral bearing capacity of various scale ratios is given in Fig. 18. When the scales of the CHFRF are 1:50, 1:10, and 1:1, the variations in lateral bearing behavior are the same, and the normalized lateral bearing capacity values are 3.07, 3.04, and 3.00, respectively, indicating that the normalized lateral bearing capacity decreases slightly with increasing scale.

When the effect of the elasticity modulus of the sand and the elasticity modulus of the CHFRF is considered in the scale analysis, the normalized lateral bearing capacities of various scale ratios are close to each other. This indicates that although the stress state in the sand varies with scale, assigning the corresponding elastic modulus to the sand based on the scale of the foundation allows model test results to be applied to actual engineering practice. The elastic modulus of sand at various scale ratios and the elastic modulus of the CHFRF can be calculated as (19)

$$\sigma_m = \frac{\sigma_p}{r_{scale}} \tag{19}$$

where the σ_m is the elastic modulus of the sand or CHFRF in the model test; the σ_p is the pressure of the sand or CHFRF in the prototype; the r_{scale} is the scale ratio.

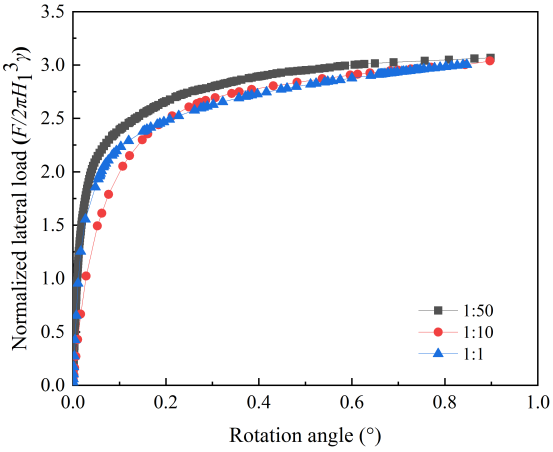

Fig. 18 The normalized lateral load against rotation angle

Fig. 19 gives the sand deformation around the CHFRF in the limit state. The lateral displacement of the CHFRF decreases from top to bottom along the loading rod, indicating that the CHFRF rotates under lateral load. This leads to sand deformation on the front side of the CHFRF (where the loading direction defines the front side), and local shear failure occurs in the sand in front of the CHFRF.

Although the failure mode of the CHFRF is almost identical at various scales, the sand deformation range differs significantly. At a scale ratio of 1:50, the range is largest (approximately 2 times the CHFRF diameter). At scales of 1:10 and 1:1, the deformation range is about 1.5 times the CHFRF diameter. This is because the small-scale foundation stiffness exceeds that of the prototype. The greater the deformation range of the sand around the CHFRF, the more sand participates in resisting the lateral load. Therefore, in practical engineering, the influence of the deformation range of the soil around the CHFRF should be taken into account. Based on the detailed geotechnical investigation data, the diameter of the CHFRF and the loading eccentricity should be adjusted to mobilize more soil to resist the lateral load.

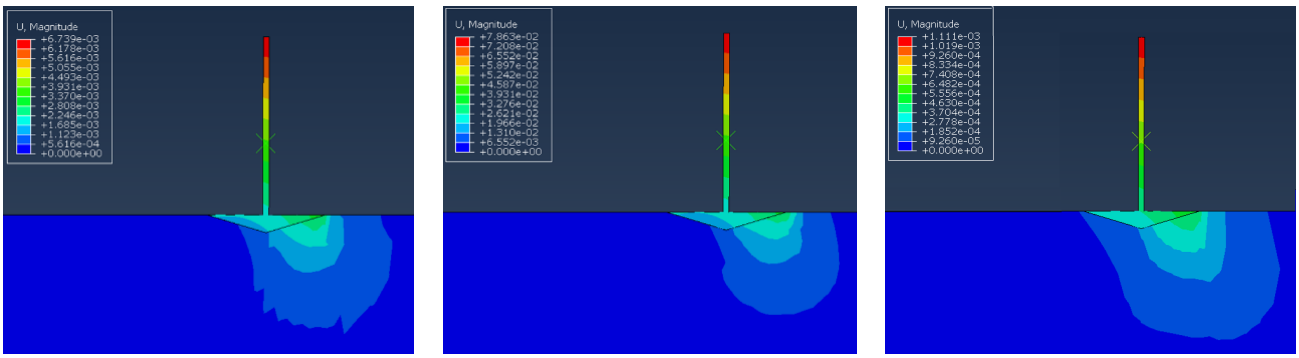

(a) 1:1 (b) 1:10 (c) 1:50

Fig. 19 Sand deformation around the CHFRF

6. Discussion

This study demonstrates that the CHFRF offers a promising alternative for onshore wind turbines, combining high lateral bearing capacity with significant material savings and reduced excavation waste, thereby lowering economic and environmental costs. However, the material of the CHFRF model in this paper is steel, which differs from the practical engineering. Wang et al. [17, 21] have conducted in-situ CT monitoring to study the evolution of the initial damage. Results show that the peak stress of the micro steel fiber specimens with a dosage of 2.0% increased by approximately 11%, and the ultimate strain increased by 65%, achieving the optimal balance of strength and toughness.

Besides, the stiffness of the CHFRF will also be changed under long-term cyclic loading, leading to significant changes in the ultimate lateral bearing capacity and the cumulative displacement. Although numerical simulations were conducted to investigate the scale effect on the lateral bearing behavior of the CHFRF, stress-level differences between the model and prototype were not considered. Refined numerical simulations will be performed in the future to investigate fatigue failure, foundation stiffness, and the scale effect on the lateral bearing capacity.

7. Conclusions

This paper studies the new type of gravity wind power foundation, CHFRF. A series of model tests and numerical simulations were conducted on the CHFRF with various aspect ratios to investigate the lateral bearing capacity. The movement law of the rotation center of CHFRF under monotonic load was revealed for the first time. A calculation method for the ultimate equilibrium of lateral bearing capacity based on the measured earth pressure distribution was proposed. The main conclusions are as follows:

(1) The lateral bearing capacity of the CHFRF increases with increasing aspect ratios and decreasing load eccentricity. The lateral bearing capacity of CHFRF is higher than that of circular foundations, indicating that CHFRF has an advantage in terms of lateral bearing capacity.

(2) The rotation center of the CHFRF moves upward as the rotation angle increases, and is located at 0.5 to 0.65H_1 before the failure of the CHFRF. Under the limiting condition, the distance from the rotation center to the top plate x/H_1 decreases with increasing the loading eccentricity and aspect ratio.

(3) Explicit integration of sidewall friction into the mechanical model. Based on the earth pressure distribution test, a method of predicting the lateral bearing capacity of the CHFRF is proposed based on the limit equilibrium method. The model test data are in good agreement with the calculation results, indicating that this method is reliable.

(4) The normalized numerical simulation data and the test data match well. The relationship between the test results and the practical engineering is established through numerical simulation, which indicates that the model test data can provide guidance for practical engineering.

Acknowledgments

This study was financially supported by the National Natural Science Foundation of China (Grant No. 52371301; 52471289)

Conflicts of Interest

The authors declare no conflict of interest.

References

[1] M. Shahraki, A. Tessari, C. Bolisetti, E. Kurt, and K. Kim, “Experimental Study on Sliding at the Soil-Structure Interface of a Shallow Foundation,” Geotechnical Testing Journal, vol. 47, no. 2, pp. 521-538, 2024.

[2] J. Rybak, “Foundations of wind power plants-challenges in designing and execution of construction work,” First

International Conference on Advances in Physical Sciences and Materials, IOP Publishing Ltd, vol. 1706, article no. 012130, 2020.

[3] W. Liu, "Design and Construction Technology of Wind Turbine Foundations for the 150 MW Qingfeng Wind Farm in Duyun, Guizhou," Yunnan Water Power, no. 3, pp. 110-119, 2021.

[4] J. B. Anderson, F. C. Townsend, and L. Rahelison, "Load Testing and Settlement Prediction of Shallow Foundation," Journal of Geotechnical and Geoenvironmental Engineering, vol. 133, no. 12, pp. 1494-1502, 2007.

[5] X. H. Gao, W. P. Tian, J. C. Li, H. L. Qi, S. Y. Li, and Z. P. Zhang, "Research on the Stress and Deformation Characteristics of Circular Foundation Pit during Excavation in Sand Soil," Advances in Materials Science and Engineering, vol. 2023, no. 6, article no. 3008695, pp. 1-22, 2023.

[6] D. Y. Li, H. B. Zhai, and Y. K. Zhang, Cone-Shaped Hollow Flexible Reinforced Concrete Foundation and Its Construction Steps, CN Patent, ZL201410654765.8, 2015.

[7] B. P. Sethy, C. Patra, B. M. Das, and K. Sobhan, "Bearing Capacity of Circular Foundation on a Sand Layer of Limited Thickness Under Eccentrically Inclined Loading," Soil Mechanics and Foundation Engineering, vol. 57, no. 6, pp. 452-457, 2021.

[8] Z. W. Deng, Q. F. Gao, H. Dong, and L. X. Li, "Dynamic Responses of the Shallow Foundation of an Onshore Wind Turbine," International Journal of Physical Modelling in Geotechnics, Vol. 19, no. 5, pp. 247-260, 2018.

[9] Z. W. Deng, Z. J. Fan, Y. M. Zhou, and P. Y. Deng, "Study on Dynamic Response Characteristics of Circular Extended Foundation of Large Wind Turbine Generator," Sustainability, vol. 14, no. 21, article no. 14213, 2022.

[10] A. Z. El-Wakil, "Horizontal Capacity of Skirted Circular Shallow Footings on Sand," Alexandria Engineering Journal, vol. 49, no. 4, pp. 379-385, 2010.

[11] A. B. Cerato and A. J. Lutenegger, "Scale Effects of Shallow Foundation Bearing Capacity on Granular Material," Journal of Geotechnical and Geoenvironmental Engineering, vol. 133, no. 10, pp. 1192-1202, 2007.

[12] D. Y. Li, S. S. Li, and Y. K. Zhang, "Cone-Shaped Hollow Flexible Reinforced Concrete Foundation (CHFRF) – Innovative for Mountain Wind Turbines," Soils and Foundations, vol. 59, no. 5, pp. 1172-1181, 2019.

[13] S.S. Li, Y. K. Zhang, and D. Y. Li, "Capacity of Cone-Shaped Hollow Flexible Reinforced Concrete Foundation (CHFRF) in Sand Under Horizontal Loading," Advances in Materials Science and Engineering, vol. 2020, article no. 6346590, 2020.

[14] Y. Zhang, D. Y. Li, H. Liang, and Y. K. Zhang, "Model Tests on Horizontal Bearing Capacity and Earth Pressure Distribution of Hollow Cone-Shaped Foundation Under Horizontal Monotonic Loading," Rock and Soil Mechanics, vol. 42, no. 5, pp. 1404-1412, 2021.

[15] D. Y. Li, J. Y. Hu, and Y. K. Zhang, "Bearing Behavior of Cone-shaped Hollow Reinforced Concrete Foundation (CHRF) and the Circular Foundation for Wind Turbines under Same Reinforced Concrete Usage," Science Technology and Engineering, vol. 21, no. 25, pp. 10887-10895, 2021.

[16] S. S. Li, Y. K. Zhang, D. Y. Li, and M. Gao, "Lateral Bearing Capacity of Cone-Shaped Hollow Foundation by Using Limit Equilibrium Method," International Journal of Physical Modelling in Geotechnics, vol. 22, no. 3, pp. 157-168, 2022.

[17] C. Q. Wang and Y. L. Lu, "Strain-Variance Damage Modeling of Microfiber-Reinforced Recycled Cementitious Composites via in-Situ 4D CT and DVC," Composites Part B: Engineering, vol. 310, article no. 113172, 2025.

[18] C. Q. Wang, Y. L. Lu, Zhang Y, Z, H. X. Wu, and M. Ma, "Computed Tomography Images and Digital Volume Correlation Analysis of Microstructural Damage Evolution in Carbonated Recycled Aggregate Concrete," Construction and Building Materials, vol. 491, article no. 142761, 2025.

[19] C. Q. Wang, Y. L. Lu, Y. C. Zhang, and Z. M. Ma, "Sustainable Carbonation-Modified Microfiber-Reinforced Cementitious Composites with Synergistic Mechanical Enhancement and 3D Strain Field Analysis," Construction and Building Materials Construction and Building Materials vol. 489, article no. 142416, 2025.

[20] C. Q. Wang, J. Liu, Y. Y. Dai, and Z. M. Ma, "Elucidate CO2 Enhancement on Multiscale Mechanical Behavior and Stiffness Degradation of Fiber-Reinforced Recycled Aggregate Concrete under Cyclic Loading," Journal of Building Engineering, vol. 111, article no. 113298, 2025.

[21] C. Q. Wang, J. Guo, F. Li, Y. C. Zhang, and Z. M. Ma, "Characterization of Failure Modes and Mechanical Behavior of Micro-Fiber-Reinforced Recycled Aggregate Concrete under Hopkinson Pressure Bar and in-Situ CT Techniques," Construction and Building Materials, vol. 458, article no. 139726, 2025.

[22] Code for Design of Building Foundations, GB/T 500007-2011, Ministry of Housing and Urban-Rural Development of the People's Republic of China, 2011.

[23] S. S. Li, D. Y. Li, and Y. F. Gao, "Determination of Maximum and Minimum Void Ratios of Sands and Their Influence

Factors," Chinese Journal of Geotechnical Engineering, vol. 40, no. 3, pp. 554-561, 2018.
[24] R. B. Kelly, G. T. Houlsby, and B. W. Byrne, "A Comparison of Field and Laboratory Tests of Caisson Foundations in Sand and Clay," Géotechnique, vol. 56, no. 9, pp. 617-626, 2006.
[25] Y. K. Zhang, D. Y. Li, and Y. F. Gao, "Earth Pressures on Modified Suction Caisson in Saturated Sand Under Monotonic Lateral Loading," Journal of Renewable and Sustainable Energy, vol. 8, no. 5, article no. 053312, 2016.
[26] Y. K. Zhang, Y. Chen, D. Y. Li, X. Y. Hou, and Y. Lai, "Lateral Bearing Characteristics of Modified Suction Caisson Embedded in Layered Soil," Applied Ocean Research, vol. 158, article no. 104572, 2025.
[27] M. M. Liu, M. Yang, and H. J. Wang, "Study on Subgrade Reaction and Punching of Circular Spread Foundation for Onshore Wind Turbines," Acta Energiae Solaris Sinica, vol. 36, no. 5, pp. 1130-113, 2015.
[28] Code for Geotechnical Investigations of Urban Rail Transit, GB 50307-2012, Ministry of Housing and Urban-Rural Development of the People's Republic of China, 2012.